

---

# WHEN NETWORK ARCHITECTURE MEETS PHYSICS: DEEP OPERATOR LEARNING FOR COUPLED MULTIPHYSICS

---

Kazuma Kobayashi<sup>\*1,3</sup>, Jaewan Park<sup>\*1,2</sup>, Qibang Liu<sup>1,4</sup>, Seid Koric<sup>1,2</sup>, Diab Abueidda<sup>1,5</sup>, and Syed Bahauddin Alam<sup>1,3</sup>

<sup>1</sup>National Center for Supercomputing Applications, University of Illinois at Urbana-Champaign, 1205 W. Clark St., Urbana, IL, 61801, USA

<sup>2</sup>The Grainger College of Engineering, Mechanical Science and Engineering, University of Illinois at Urbana-Champaign, 1206 W Green St, Urbana, IL 61801, USA

<sup>3</sup>The Grainger College of Engineering, Nuclear, Plasma & Radiological Engineering, University of Illinois at Urbana-Champaign, 104 South Wright Street, Urbana, IL 61801, USA

<sup>4</sup>Department of Industrial and Manufacturing Systems Engineering, Kansas State University, Manhattan, KS 66506, USA

<sup>5</sup>Civil and Urban Engineering Department, New York University Abu Dhabi, UAE

## ABSTRACT

Scientific applications increasingly demand real-time surrogate models that can capture the behavior of strongly coupled multiphysics systems driven by multiple input functions, such as in thermo-mechanical and electro-thermal processes. While neural operator frameworks, such as Deep Operator Networks (DeepONets), have shown considerable success in single-physics settings, their extension to multiphysics problems remains poorly understood. In particular, the challenge of learning nonlinear interactions between tightly coupled physical fields has received little systematic attention. This study addresses a foundational question: *should the architectural design of a neural operator reflect the strength of physical coupling it aims to model?* To answer this, we present the first comprehensive, architecture-aware evaluation of DeepONet variants across three regimes: single-physics, weakly coupled, and strongly coupled multiphysics systems. We consider a reaction–diffusion equation with dual spatial inputs, a nonlinear thermo-electrical problem with bidirectional coupling through temperature-dependent conductivity, and a viscoplastic thermo-mechanical model of steel solidification governed by transient phase-driven interactions. Two operator-learning frameworks, the classical DeepONet and its sequential GRU-based extension, S-DeepONet, are benchmarked using both *single-branch* and *multi-branch* (MIONet-style) architectures. Our results demonstrate that architectural alignment with physical coupling is crucial: single-branch networks significantly outperform multi-branch counterparts in strongly coupled settings by leveraging shared latent representations, whereas multi-branch encodings offer advantages for decoupled or single-physics problems. Once trained, these surrogates achieve full-field predictions up to  $1.8 \times 10^4$  times faster than high-fidelity finite-element solvers, without compromising solution accuracy. These findings introduce a coupling-aware design principle for neural operators, offering a practical foundation for deploying DeepONet-based surrogates in real-time digital twins, design optimization, and uncertainty quantification across complex multiphysics domains.

**Keywords** Deep Operator Neural Networks · Multiple Inputs · Multiphysics · Coupled Solutions

## 1 Introduction and Previous Work

Machine learning (ML) has rapidly transformed computational science by enabling efficient data-driven approximations of complex physical processes. Among these, artificial neural networks (NNs), inspired by the architecture of biological neural systems, have shown particular promise for physics-based modeling tasks in engineering and the physical sciences. When trained on representative datasets, NNs can learn input-output mappings that approximate the behavior

of numerical solvers, thereby serving as surrogate models. This surrogate capability has been successfully applied to a wide range of tasks, including sensitivity analysis, uncertainty quantification [1], and inverse design in domains such as cardiac electrophysiology [2], optical assemblies [3], advanced manufacturing [4, 5, 6], and multi-physics engineering problems [7, 8].

To reduce the need for large volumes of simulation data, physics-informed neural networks (PINNs) have been developed to incorporate governing physical laws directly into the training process [9, 10, 11, 12, 13]. PINNs embed differential equations and boundary conditions within the loss function, enabling training with minimal to no labeled solution data. Despite their theoretical appeal, PINNs often face practical limitations, including high computational cost during training and reduced accuracy in high-dimensional, stiff, or multi-scale problems [14, 15]. Their performance also degrades when modeling strongly coupled or path-dependent systems, where architectural specialization becomes essential.

These challenges have motivated the development of neural operator learning frameworks, which aim to approximate mappings between infinite-dimensional function spaces. Unlike traditional NNs that operate on fixed-dimensional vectors, neural operators generalize across discretizations, allowing the learned models to predict entire solution fields over arbitrary spatial and temporal grids [16]. This property makes them particularly attractive for scientific and engineering applications where simulation cost, geometric variability, and resolution flexibility are critical. Neural operators build on the theoretical foundation that neural networks can serve as universal approximators of nonlinear operators [17], and recent advances have demonstrated their ability to deliver substantial speedups while maintaining accuracy across diverse PDE settings [18]. Ongoing work extends neural operators to variable geometries via diffeomorphic transformations [19] and embeds physical-law constraints through physics-informed neural operators (PINO) [20]. Further developments, such as the Physics-Informed Parallel Neural Operator (PIPNO) [21], enable data-free modeling by enforcing governing equations directly during training, while architectures like the Codomain Attention Neural Operator (CoDA-NO) [22] enhance generalization across coupled multi-physics systems through self-supervised attention mechanisms in the output space. Collectively, these advances position neural operators as a promising foundation for real-time surrogates in complex simulations, particularly in settings involving multi-resolution, geometry variability, or coupled field interactions.

*However, their application to strongly coupled multiphysics systems remains limited and poorly understood.* Most existing DeepONet-based studies target single-physics problems and do not address the challenge of learning nonlinear interactions across tightly coupled variables. Answering this question is crucial for unlocking the potential of neural operators in time-sensitive, safety-critical simulations where surrogate accuracy and efficiency are paramount.

Two representative frameworks have emerged among neural operator architectures: the Fourier Neural Operator (FNO) and the Deep Operator Network (DeepONet). The FNO, introduced by Li et al. [23], employs the fast Fourier transform (FFT) to encode input functions in the spectral domain. FNO achieves discretization-invariant learning and strong generalization across varying resolutions and geometries by performing global convolutions in Fourier space. However, its reliance on periodic boundary conditions and global basis functions can hinder its ability to capture localized features or sharp discontinuities. To address these limitations, several variants have been proposed, including Conv-FNO, which integrates UNet-style local feature extraction; AM-FNO, which amortizes kernel parameterization for efficient learning; and the Wavelet Neural Operator (WNO), which replaces FFTs with discrete wavelet transforms to improve spatial localization and multiscale representation [24, 25, 26]. These architectures have shown strong performance in regular domains, such as those encountered in subsurface flow and CO<sub>2</sub> geological storage simulations. To mitigate spectral bias in multi-scale systems, hierarchical attention mechanisms and scale-adaptive receptive fields have been integrated into recent designs, substantially improving derivative approximation and fine-scale resolution [27, 28].

In parallel, DeepONet offers an alternative operator-learning architecture built on a dual-network structure. Initially proposed by Lu et al. [29], DeepONet employs a branch network to encode the input function and a trunk network to process spatial or spatiotemporal coordinates. The outputs of both networks are combined to directly predict the solution field, enabling high-resolution field estimation even in complex geometries. DeepONet has since been extended to incorporate physical constraints (PI-DeepONet), separable structures (Sep-PI-DeepONet), and recurrent mechanisms for time-dependent problems (Sequential DeepONet) [30, 31, 32]. These variants have been successfully applied in nonlinear solid mechanics, fracture mechanics, aerodynamics, seismology, fluid flow, and heat transfer [33, 34, 35, 36, 37, 38, 39, 40, 41, 42, 43]. Performance improvements have also been achieved through orthonormalized two-stage training [44], enriched architectures for moving-solution operators [37], and multifidelity frameworks that leverage low-fidelity simulations to improve high-fidelity predictions with limited training samples [45]. Notably, U-DeepONet has demonstrated faster training and improved generalization compared to U-FNO for multiphase flow problems [46], while DeepM&Mnet introduces a modular, plug-and-play design for modeling coupled multi-physics systems with orders-of-magnitude speedup over traditional CFD solvers [47, 48]. Similarly, Fourier-MIONet, a multiple-branch DeepONet architecture that integrates Fourier-mode filtering into its latent representations, has

achieved substantial reductions in parameter count compared to U-FNO, with minimal accuracy degradation across complex multiphase benchmarks [49]. Yet, how network architecture should adapt to different levels of inter-physics coupling remains largely unresolved, particularly for problems involving tightly interdependent variables.

The real-world utility of neural operators has been demonstrated in various industrial and high-consequence domains. For instance, FNO-based digital twins have been deployed in additive manufacturing systems to enable closed-loop feedback control and real-time process optimization [50]. Operator-learning frameworks have also been integrated into digital twins [51, 52] for nuclear reactors, providing real-time particle transport prediction and anomaly detection in high-stakes operational environments [53]. These deployments highlight the scalability, data efficiency, cross-domain generalization, and computational efficiency of neural operators in settings where traditional numerical solvers are often infeasible for real-time or high-throughput tasks.

Despite these successes, most DeepONet-based studies to date focus on single-physics systems, and their application to complex coupled physics scenarios remains nascent. Many practical systems involve strongly coupled multiphysics interactions (thermal–structural, electro-thermal, fluid–structure, etc.) [54]. Coupled multiphysics modeling is essential for accurate prediction and enhanced safety or performance, but it incurs significant computational costs; high-fidelity multiphysics simulations on fine meshes are often prohibitively slow, which hinders tasks that require rapid or repeated evaluations (e.g. sensitivity studies, uncertainty quantification, design optimization, real-time control, and digital twin updates) [5]. Consequently, it is timely to investigate whether operator-learning techniques, such as DeepONet, can serve as efficient surrogates for multiphysics systems, thereby enabling advanced analyses and real-time decision-making that are beyond the reach of conventional solvers. Indeed, initial demonstrations have shown that DeepONet surrogates can predict full-field coupled physics solutions several orders of magnitude faster than optimized finite-element simulations on HPC platforms [5]. However, applying DeepONet to strongly coupled, high-dimensional multiphysics problems introduces new challenges. The efficacy of current operator networks in multiphysics scenarios remains uncertain, with open questions about whether they can handle multiple interacting variables and capture the strong nonlinear inter-field couplings without accumulating errors [54]. In practice, existing neural operator architectures have struggled on multiphysics PDEs due to the complex interactions between physical variables and the limited availability of high-resolution coupled-training data [22]. To date, no systematic framework has been proposed to test or guide architectural selection based on coupling strength. This work addresses that gap by presenting the first systematic evaluation of operator surrogates in strongly coupled multiphysics systems, providing practical guidelines for coupling-aware design.

## 2 Methods

To evaluate how operator network architectures respond to varying levels of physical coupling and input modality, we construct three purpose-designed benchmark problems that span single-physics, weakly coupled, and strongly coupled regimes. While reaction–diffusion systems have been studied in prior work, our formulation introduces a novel two-input configuration, with both source and reaction terms modeled as heterogeneous spatial fields. This setting challenges the network’s ability to learn under spatially structured variability. The thermo-electrical benchmark captures nonlinear bidirectional interactions via temperature-dependent electrical conductivity and Joule heating, allowing us to isolate the impact of physical coupling on surrogate fidelity. Finally, we apply a recurrent operator learning framework to a viscoplastic thermo-mechanical solidification model, where stress depends on both phase evolution and thermal history. By systematically contrasting fully coupled and decoupled simulation datasets, we provide, to our knowledge, the first architectural sensitivity analysis that links physical coupling strength with the effectiveness of encoding strategies in operator learning.

### 2.1 Single Physics Reaction-Diffusion Model and Data Generation

The first benchmark problem involves a single-physics reaction–diffusion partial differential equation (PDE) (given in Equation 1), representative of a broad class of transport-dominated phenomena in physics and biology, including thermal conduction in heterogeneous media, chemical diffusion, and drug dispersion in tissue. The governing equation is given by:

$$\frac{\partial u}{\partial t} = 0.01 \nabla^2 u + u_0(x) - k(x)u \quad (1)$$

The reaction part consists of two spatially dependent functions,  $u_0(x)$  and  $k(x)$ , which contribute to the equation’s nonlinearity. They are randomly generated following a Gaussian distribution using the `gstools` [55] package. Finite element simulations were conducted to determine  $u(x, t)$  within a one-dimensional domain discretized with 127 second-order 1D elements (255 nodes total) and solved in 101 time steps, resulting in the generation of 10,000 samples,

utilizing the open-source package FEniCSx [56]. This dataset encompasses a broad spectrum of spatial input conditions provided by the two input functions, along with the corresponding full spatial-temporal solutions, also known as labels or targets.

## 2.2 Coupled Electrical Conduction and Thermal Diffusion Model and Data Generation

The first multiphysics use case is the coupled electrical conduction and thermal diffusion PDE system with multiple inputs. The coupled electrical conduction and thermal diffusion model describes the highly coupled interaction between electrical currents and heat flow in a material. These PDEs have essential applications in thermal management in electronics and semiconductor devices, batteries and energy storage systems, tissue ablation in biomedical applications, electroplating, and welding in manufacturing, among many others. The normalized governing equations for the coupled model are presented as follows:

$$\begin{cases} \frac{\partial T}{\partial t} = \nabla \cdot (k \nabla T) + Q_{\text{ext}} + Q_e \\ \frac{\partial^2 \phi}{\partial t^2} = \nabla \cdot (\gamma \nabla \phi) + \rho_e \end{cases} \quad (2)$$

Here,  $k = 0.116$  denotes the thermal conductivity,  $Q_{\text{ext}}$  represents the heat source term, and  $Q_e = \gamma |\nabla \phi|^2$  is the heat generated by electrical currents. The solution  $\phi$  is the electric potential, while  $\gamma$  refers to the electrical conductivity of the material, defined as  $\gamma = \frac{1}{1+\beta T}$  for metals, where  $\beta = 3.9$  is the temperature coefficient of resistivity. Additionally,  $\rho_e$  is the free charge density, which accounts for any non-zero net charge within the system.

In this example, the time-dependent input functions  $Q_{\text{ext}}(t)$  and  $\rho_e(t)$  were randomly generated following a Gaussian distribution using the `gstoools` [55] package. Finite element simulations were then conducted to solve for  $T$  and  $\phi$  within a one-dimensional domain consisting of 127 second-order elements over 101 time steps to generate 5000 samples, using again the open-source package FEniCSx [56]. This dataset captures a wide range of realistic temporal input conditions, enabling trained neural network models to generalize effectively across unseen input scenarios and the corresponding diverse scenarios of thermal and electrical solution fields, as well as their interactions.

## 2.3 Thermo-Mechanical Model of Steel Solidification and Data Generation

Although advancements in metal-based additive manufacturing are progressing steadily, the materials processing domain remains predominantly governed by conventional techniques, such as ingot, foundry, and continuous casting. Continuous casting accounts for more than 95% of global steel production. Experiments are constrained by the severe environment of molten steel and the numerous process variables that influence its intricate multiphysics phenomena. The progress of these established manufacturing processes mostly depends on the enhanced quantitative insights obtained from advanced multiphysics numerical models. Significant advancements in computing technology and numerical techniques over the past 30 years have enabled more realistic and precise multiphysics simulations of steel solidification processes on high-performance computing systems, utilizing specialized software in predominantly offline academic research environments. However, optimization, designs, and real-time predictions for online controls and digital twins of these processes are still primarily impossible by classical modeling methods.

We utilize the modeling output from the existing thermo-mechanical finite-element model, which incorporates a solidifying slice domain moving in the Lagrangian frame of reference down the continuous caster, to produce training and testing data for the sequential deep learning methodologies. The governing equation for the We utilize the modeling output from the existing thermo-mechanical finite-element model, which incorporates a solidifying slice domain moving in the Lagrangian frame of reference down the continuous caster, to produce training and testing data for the sequential deep learning methodologies. The governing equation for the thermal behavior of the solidifying shell is presented in Equation 3.

$$\rho \frac{\partial H}{\partial t} = \nabla \cdot (k \nabla T) \quad (3)$$

where  $\rho$  is density,  $k$  is thermal conductivity, and  $H$  is specific enthalpy, including the latent heat during phase transformations, such as in solidification and transition between different phases, such as  $\delta$ -ferrite to austenite. In solidification mechanical problems, inertial effects are negligible, so the quasi-static mechanical equilibrium in Equation 4 is appropriate:

$$\nabla \cdot \sigma(\mathbf{x}) + \mathbf{b} = \mathbf{0} \quad (4)$$

where  $\sigma$  is the Cauchy stress tensor, and  $\mathbf{b}$  is the body force density vector. The rate representation of total strain in this thermo-elastic-viscoplastic model is given as follows:

$$\dot{\epsilon} = \dot{\epsilon}_{el} + \dot{\epsilon}_{ie} + \dot{\epsilon}_{th} \quad (5)$$

where  $\dot{\epsilon}_{el}$ ,  $\dot{\epsilon}_{ie}$ ,  $\dot{\epsilon}_{th}$  are the elastic, inelastic, and thermal strain rate tensors, respectively. Thermal strain depends on the temperature solution and thermal expansion coefficient,  $\alpha$ , which is also a temperature-dependent property at high steel temperatures. The constitutive equation relates the stress and strain rates:

$$\dot{\sigma} = \mathbf{D} : (\dot{\epsilon} - \alpha \mathbf{I} \dot{T} - \dot{\epsilon}_{ie}) \quad (6)$$

where  $\mathbf{D}$  is the fourth-order tensor containing the isotropic elastic temperature-dependent constants, and  $\mathbf{I}$  is the identity tensor. At high temperatures near the solidification or melting point, steel alloys exhibit significant time- and temperature-dependent plastic behavior, including phase transformations. Kozłowski et al. [57] created a visco-plastic constitutive equation to model the austenite phase of steel, relating inelastic strain to stress, strain rate, temperature, and steel grade via carbon content, Equation 7:

$$\dot{\epsilon}_{ie} [\text{s}^{-1}] = f_c \left( \bar{\sigma} [\text{MPa}] - f_1 \bar{\epsilon}_{ie} |\dot{\epsilon}_{ie}|^{f_2-1} \right)^{f_3} \exp\left(-\frac{Q}{T [\text{K}]}\right) \quad (7)$$

where

$$\begin{aligned} Q &= 44,465, \\ f_1 &= 130.5 - 5.128 \times 10^{-3} T [\text{K}], \\ f_2 &= -0.6289 + 1.114 \times 10^{-3} T [\text{K}], \\ f_3 &= 8.132 - 1.54 \times 10^{-3} T [\text{K}], \\ f_c &= 46,550 + 71,400 (\%C) + 12,000 (\%C)^2. \end{aligned}$$

$Q$  is an activation energy constant in ( $K$ ) defined as activation energy in (J/mol) over gas constant (J/molK), (MPa) is Von Mises effective stress, empirical functions  $f_1$ ,  $f_2$ ,  $f_3$ , and  $f_c$  depend on absolute temperature (K), and %C is carbon content (weight percent) representing steel grade (composition). Another constitutive model, the so-called Zhu power law model [58], not shown here, was devised to simulate the delta ferrite phase with a relatively higher creep rate and weaker than the austenite phase and is applied in the solid whenever the delta-ferrite's volume fraction is more than 10%, to approximate the dominating influence of the very high-creep rates in the delta-ferrite phase of mixed-phase structures on the net mechanical behavior. This work applies the elastic-perfectly-plastic constitutive model with small yield stress above the solidus temperature  $T_{sol}$  to enforce negligible strength in those volatile zones. The highly nonlinear constitutive visco-plastic austenite or delta-ferrite models are efficiently integrated at the integration points in the UMAT subroutine [59] and linked with Abaqus [60] implicit finite element analysis (FEA) software, which in turn solves the coupled thermo-mechanical governing Equations 1 and 2 by the implicit nonlinear finite element solution methodology. The phase fraction and temperature-dependent material properties calculations for the low carbon steel grade chosen for this work with 0.09 wt%C, with solidus and liquidus temperatures  $T_{sol} = 1480.0^\circ\text{C}$  and  $T_{liq} = 1520.7^\circ\text{C}$  are also an integral part of the UMAT subroutine, and more details about this robust multiphysics model can be found in [61]. When subjected to thermal loading, generalized plane strain conditions can effectively restore a complete three-dimensional stress state in long objects, such as the continuous caster on the left side of Figure 1, which has a significant length and width. The slice domain in Figure 1 moves down the mold at casting velocity in a Lagrangian frame of reference.

Figure 2a illustrates the coupled temperature and mechanical conditions employed in addressing the associated boundary value problems (BVP) to produce training and testing data. The generalized plane strain condition in the axial ( $z$ -direction) is represented by a single row of 300 interconnected thermo-mechanical generalized plane strain 2D elements comprising 602 nodes. Additionally, a second generalized plane strain condition was applied at the lower boundary of the domain by enforcing uniform strain in the  $y$ -direction on the vertical displacements of all nodes. The thermal and mechanical boundary conditions of the solidifying slice domain are determined by time-dependent heat flux profiles emanating from the chilled surface on the left side of the domain, as well as their displacement resulting from mold taper and other thermo-mechanical interactions with the mold, also depicted in Figure 2a. The research conducted at the steel plant reveals that the displacement profile has an upward trend due to mold taper. In contrast, the thermal flux demonstrates a general downward trajectory due to transient heat transfer cooling. A radial basis interpolation utilizing the Gaussian function is employed to interpolate various temporal points randomly defined within expected profile value ranges, accommodating additional fluctuations and data noise observed in actual flux and displacement profiles due to abrupt changes in contact conditions and interfacial heat transfer between the mold and steel surfaces. They cover all potential thermo-mechanical boundary condition scenarios in which the solidifying shell would encounter at

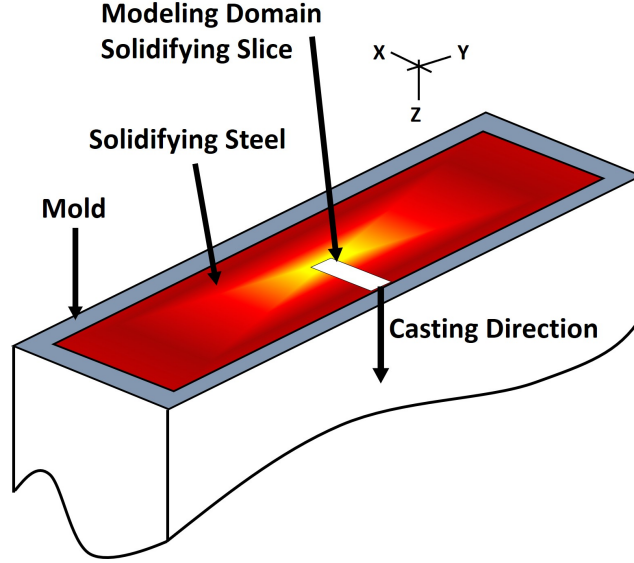


Figure 1: Slice Modeling Domain in Caster. Adapted and modified from a prior work by the authors [32].

its cooled surface while descending the caster. Besides data from fully coupled analysis, data samples were generated from uncoupled analysis whose BC-s were depicted in Figure 2b, where the single temperature solution was passed into a separate mechanical analysis, thus providing us an opportunity to study further how S-DeepONet learns stress solution for uncoupled analysis where stress solution depends on its mechanical (displacement) input only. Although simplified and less accurate, such uncoupled analysis has some practical meaning, where for a fixed heat flux profile and thus fixed temperature solution, the mechanical effects of mold's thermal distortion and taper on a solidifying domain can be studied independently for residual stress generation.

The computed temperature and stress fields are the intended targets for the S-DeepONet network. A total of 5494 data points were generated using the high-throughput and parallel solver capabilities of the high-performance cluster Delta [62] hosted at the National Center for Supercomputing Applications (NCSA). Besides fully coupled analysis, a similar number of data samples were generated from uncoupled analysis, where the single temperature solution was passed into a separate mechanical analysis, thus providing an opportunity to study further how S-DeepONet learns the stress solution for uncoupled analysis, where the stress solution depends on its mechanical (displacement) input only.

## 2.4 DeepONet Architectures

DeepONet, initially introduced by Lu et al. [29], is an artificial neural network engineered to learn nonlinear operators that transform between functional spaces, including those that denote integral operators, partial differential equations (PDEs), or dynamical systems. In a functional space  $U$ ,  $u \in U$  represents the input parameters (i.e., input functions), and  $s \in S$  refers to an unknown PDE solution in the functional space  $S$ .

We assume a single solution  $s = s(u)$  in  $S$  for every  $u \in U$ , which is also subject to the boundary conditions. As a result, the mapping solution operator  $G : U \rightarrow S$ , evaluated at continuous spatiotemporal coordinates  $\xi$  can be defined as:

$$G(u)(\xi) = s(u)(\xi) \quad (8)$$

In its original form [29] schematically represented in Figure 3, DeepONet architecture consisted of two forward fully connected neural networks (FNNs): a branch net, that encodes the input function  $u$  at fixed sensor locations, to  $B_h$  output, and a trunk net, that encodes  $T_{nh}$  information relating to the  $n$  spatiotemporal coordinates where the output solution is defined, to  $T_{nh}$  output. Dimension index  $h$  represents the hidden output dimension of the branch and trunk networks. DeepONet considers both  $u$  and  $\xi$  and predicts a solution by combining their encoded outputs via a dot product over the hidden dimension  $h$ , including bias  $\beta$ . It then compares these outputs to the target solutions (labels) provided by classical numerical analysis and calculates the loss function, which represents the prediction error. Subsequently, during the backpropagation process, the gradient of the loss function with respect to the trainable parameters  $\theta$  (weights and biases) in both networks is computed, and the optimizer reduces the loss value by modifying

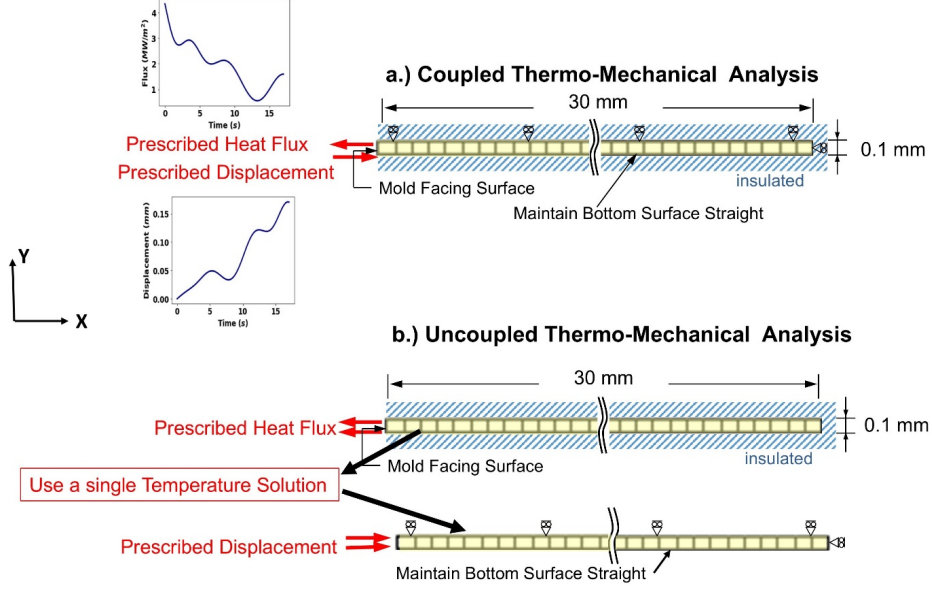


Figure 2: Thermal and Mechanical BVP: (a) Coupled, (b) Uncoupled

the trainable parameters (weights and biases). After completing a sufficient number of feedforward and backpropagation iterations, referred to as epochs, DeepONet can predict solutions across the entire domain, also known as solution fields.

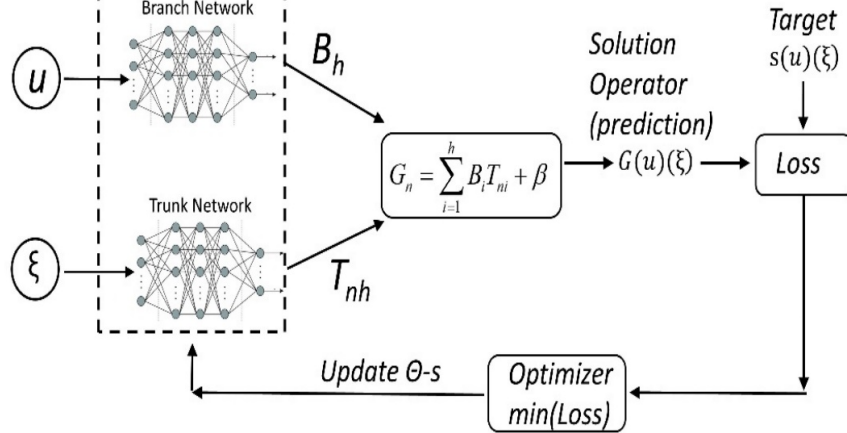


Figure 3: Original DeepONet Architecture

In cases of multiple input functions, one can read and encode them jointly in a single branch network, or each input function can have its own branch network that encodes it independently. The encoded outputs from branches are joined by the element-by-element tensor (Hadamard) product before the dot product with trunk output, as first proposed in MIONet by Jin et al [63]. In that work, single-physics PDE examples with multiple input functions were trained, and the advantage of MIONet in terms of prediction accuracy was demonstrated over single-branch DeepONet. However, that work did not consider multiphysics cases where physics phenomena are coupled and tightly dependent on each other including the path-dependent behavior, where the final state of a such system doesn't just depend on where it ends up, but also on how it got there through the order of elements in sequential input functions.

In multiphysics problems, the underlying physical processes are often driven by sequential input functions, and the characteristics of the governing physics, such as path dependency in plastic deformation, necessitate a complete load history to determine the system's final state accurately. Since the original DeepONet architecture with a feedforward

fully connected neural network (FNN) in the branch does not capture the sequential nature of its input, the authors recently introduced the sequential DeepONet (S-DeepONet) [32], which employs a gated recurrent unit (GRU) based encoder-decoder model in the branch network, replacing the conventional feedforward neural network (FNN) model for better encoding sequential input functions. Gated Recurrent Units are more suitable for sequential learning than standard recursive neural networks because they address vanishing gradient issues with gating mechanisms, thereby enabling the learning of long-term dependencies. The S-DeepONet model demonstrated significantly enhanced predictive accuracy [32] compared to the original DeepONet, albeit with an extended training duration. Figure 4 shows the architecture with a single-branch that encodes both inputs  $d$  and  $f$  together in a coupled fashion through a series of GRU cells arranged in an encoder-decoder fashion, resulting in encoded branch output  $B_h$  with hidden dimension size HD (or  $h$ ). Similarly, the trunk network takes  $n$  input domain coordinates and encodes them into its multidimensional output  $T_{nhc}$ , where  $c$  represents the number of output solution fields predicted simultaneously, i.e.,  $c = 2$ , corresponding to temperature and stress. The encoded outputs from the branch and trunk are joined via a dot product to form the final S-DeepONet prediction  $G_{nc}$  via a dot product along the hidden dimension, including bias  $\beta$ .

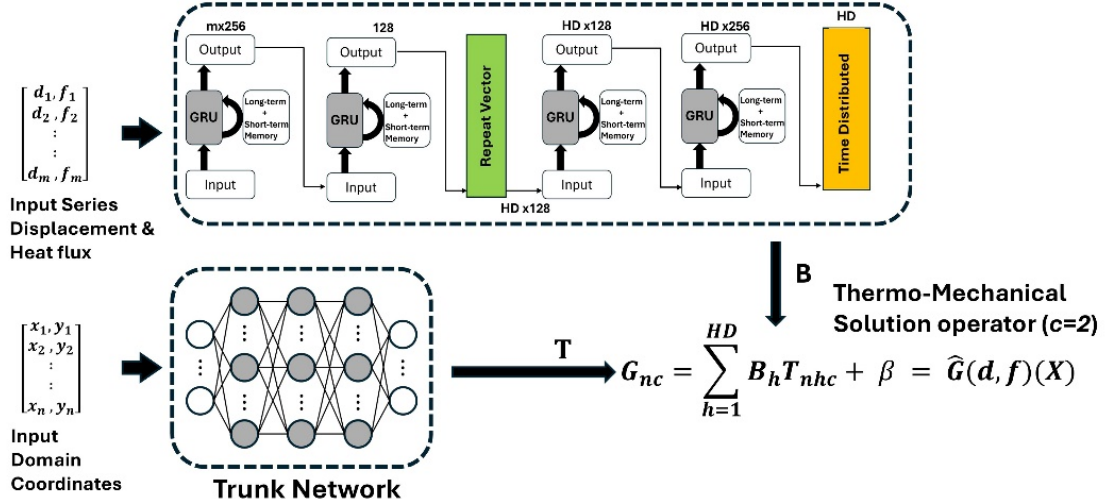


Figure 4: S-DeepONet, Single-Branch

Inspired by MIONet [63], which showed increased prediction accuracy for encoding multiple inputs in single-physics problems, a novel variant of S-DeepONet that encodes thermal and mechanical inputs in separate encoder-decoder GRU thermal and mechanical branches and then joins their outputs  $B_d$  and  $B_m$  via element-by-element (Hadamard) tensor product, denoted by  $\odot$ , is devised and represented in Figure 5. Identical S-DeepONet architectures were trained on the thermo-electrical multiphysics example from Section 2.1, using the heat source and charge density input sequences to branch, while the spatiotemporal  $x, t$  coordinate pairs were input into the trunk.

### 3 Results

The data generated from a single physics reaction-diffusion model is used to train both single-branch and two-branch (MIONet-based) DeepONet models. Multiphysics data generated from coupled and uncoupled thermo-electrical and thermal-mechanical models is used to train a single-branch S-DeepONet and a two-branch (MIONet-based) S-DeepONet. In all cases, 80% of the data is used for training and 20% is reserved for testing. The DeepXDE library [64], with a TensorFlow backend, was used as the deep learning framework. All training tasks were executed on an Nvidia A100 GPU within the Delta HPC system [62].

#### 3.1 Single Physics: Reaction-diffusion Model

$L_2$  relative errors between the finite element method (ground truth)  $S_{FE}$  and predicted solutions  $S_{pred}$  were used throughout this work to evaluate the model performance:

$$L_2 = \frac{\|S_{FE} - S_{pred}\|_2}{\|S_{FE}\|_2} \quad (9)$$



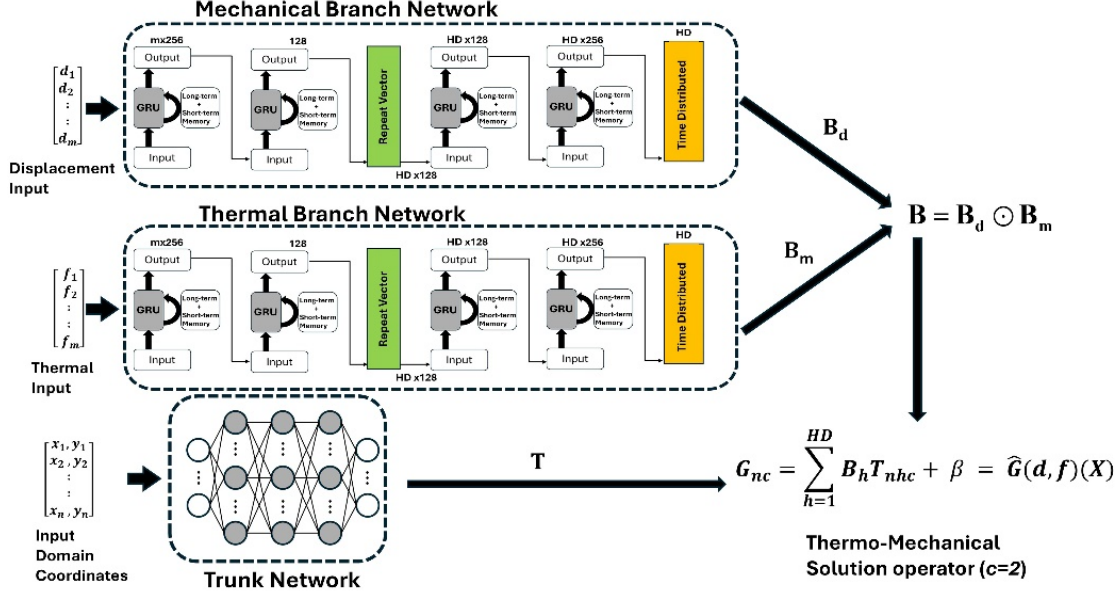


Figure 5: S-DeepONet, Two-Branch (MIONet)

$\| \cdot \|_2$  represents the level-2 norm, which for a vector  $\mathbf{v} = [v_1, v_2, \dots, v_n]$  is defined as:

$$\|\mathbf{v}\|_2 = \sqrt{\sum_{i=1}^n v_i^2}. \quad (10)$$

For 20% of the dataset, set aside for testing and never used to train DeepONet, the mean  $L_2$  error was 3.40% for a single-branch and 2.55% for a two-branch MIONet. The architecture is a classical DeepONet with branches equipped with fully connected (FNN) networks, as the input functions  $u_0(x)$  and  $k(x)$  are of spatial rather than temporal nature and do not induce path-dependent responses. Figure 6 shows the full spatial-temporal solution field comparison between single-branch and two-branch models for 55th (top row), 85th (middle row), and 99th percentile (bottom row) test samples, with 0% corresponding to the best test sample characterized by the smallest error, and 99% corresponding to the worst test sample, characterized by the largest error.

It can be observed, particularly from the contours of absolute errors, that the MIONet-based DeepONet, when reading and encoding spatial input functions separately, exhibits visibly less error in the domain compared to the single-branch DeepONet. This is entirely in agreement with what Jin et al. [63] observed in their original MIONet work.

### 3.2 Multiphysics: Thermo-electrical Model

Since both multiphysics cases utilize a temporal input function, resulting in path-dependent final thermal and mechanical solution responses, S-DeepONet rather than DeepONet architectures were employed. As mentioned before, in such a scenario, S-DeepONet provides significantly more accurate predictions compared to DeepONet, as confirmed in [32]. Figure 7 compares the predicted and target electrical potential values. At the same time, Figure 8 presents the temperature results at the final time step along the domain direction for coupled multiphysics data using both the single-branch and two-branch (MIONet) S-DeepONet models. The single-branch S-DeepONet implementation yields temperature and electrical potential solutions that align more closely with the FEM solution (target) compared to the two-branch S-DeepONet. Additionally, the histogram of test error distributions in Figure 8 highlights the superior accuracy of the single-branch implementation over the two-branch implementation, particularly for the electrical potential. The two-branch predictions for electrical potential (represented by blue columns) exhibit a long tail, indicating larger error areas.

The uncoupled data model with a single-temperature solution passed into the electrical conduction represents a significantly less challenging case for predicting electrical potential distribution, which only depends on the charger density  $\rho_e$ , and a single electric potential distribution is passed into the heat diffusion equation for predicting the

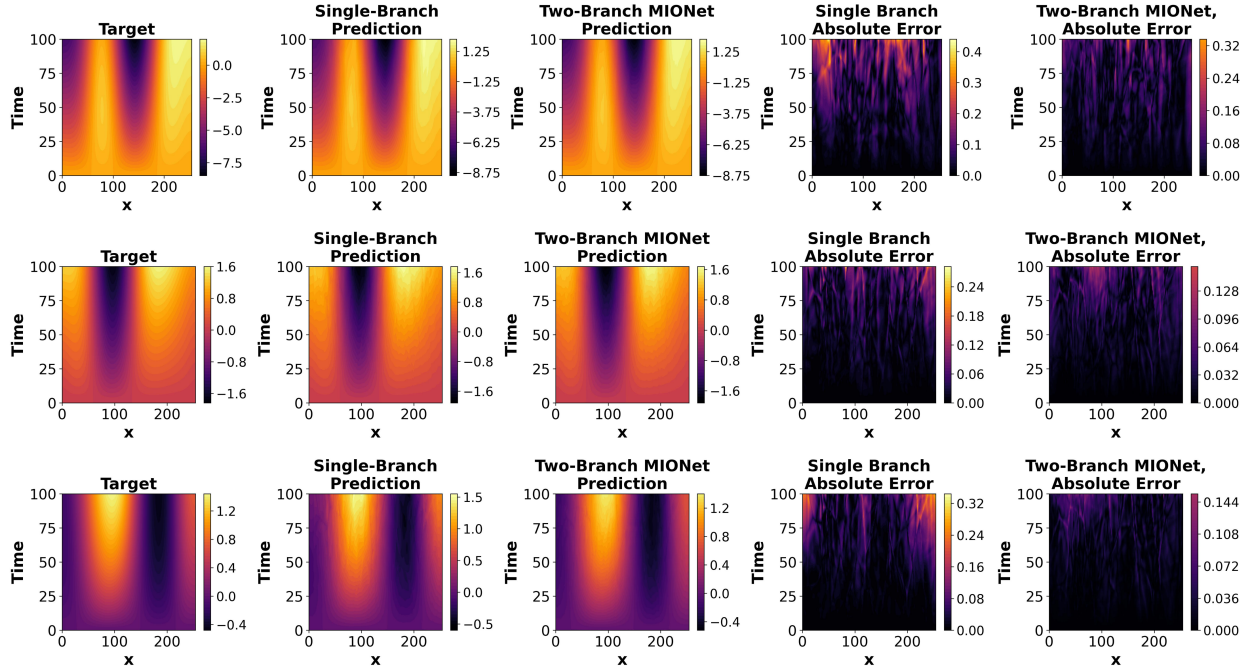


Figure 6: Single and Two-Branch DeepONet Comparison for 55th (top row), 85th (middle row), and 99th (bottom row) percentile test samples, ranked by error size

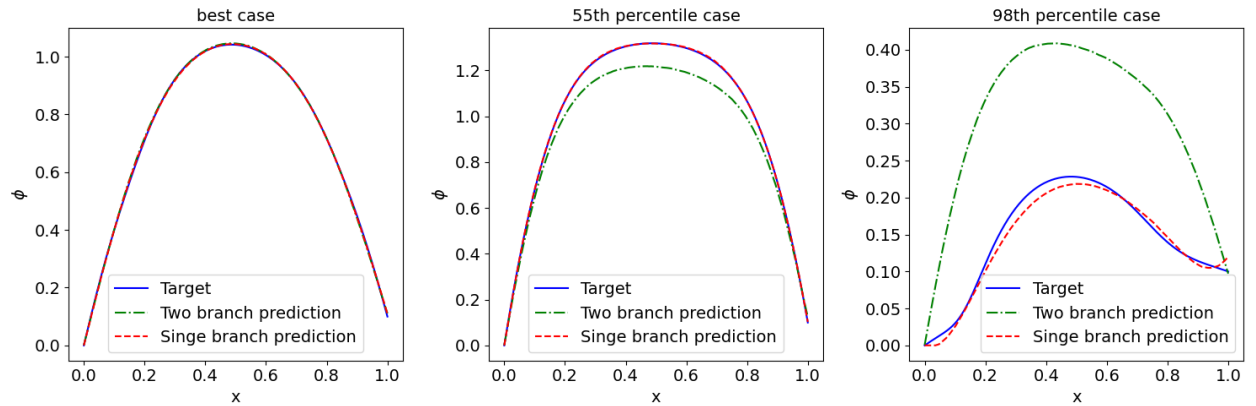


Figure 7: Electrical Potential Comparison, Coupled Multiphysics Data

temperature, which only depends on the external heat source  $Q_{\text{ext}}$ . The corresponding histogram of test errors in Figure 9 reveals that the data from that uncoupled dual physics slightly favors the 2-branch (MIONet) model, which reads and encodes thermal and electric inputs separately.

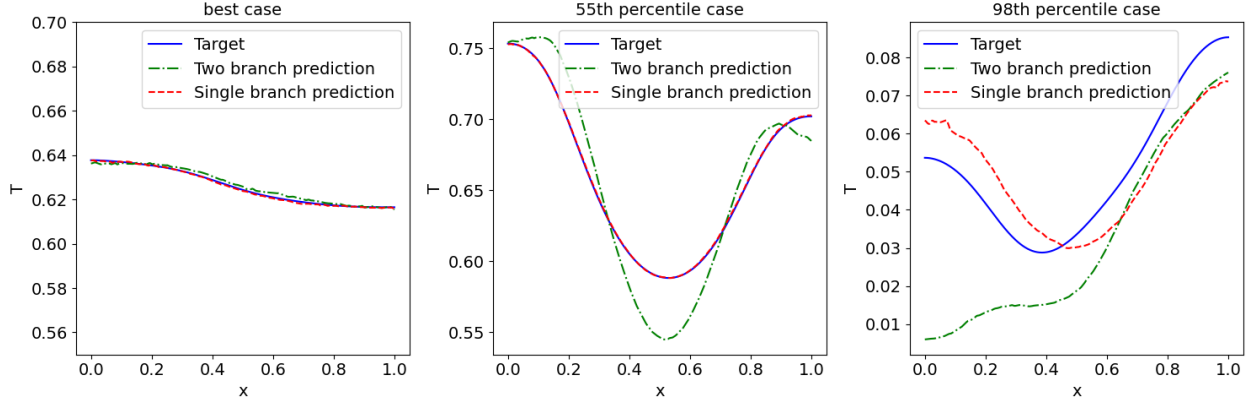


Figure 8: Temperature Comparison, Coupled Thermo-Electrical Physics

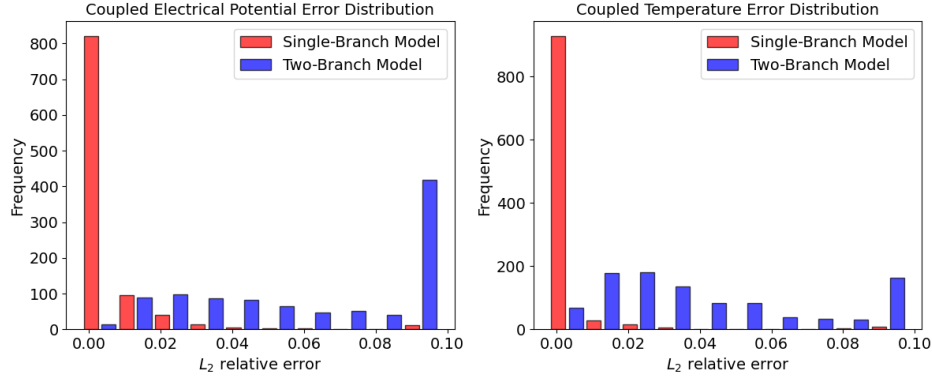


Figure 9: Histogram of Test Errors, Coupled Thermo-Electrical Physics

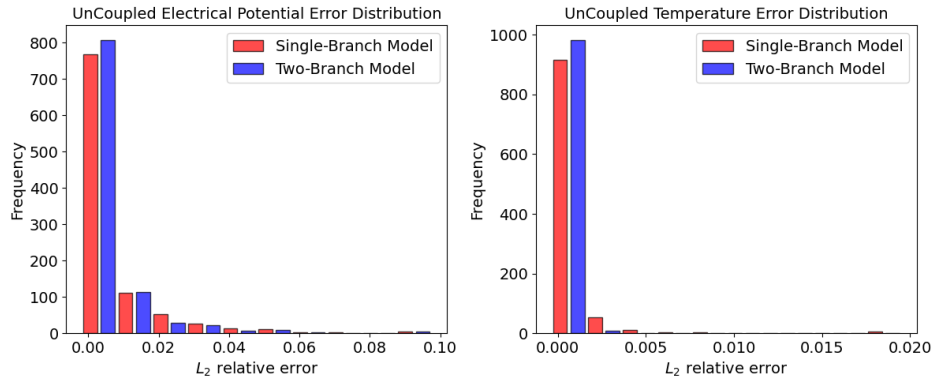


Figure 10: Histogram of Test Errors, Uncoupled Thermo-Electrical Physics

Tables 1 and 2 summarize these  $L_2$  relative error results. The single-branch S-DeepONet, which reads both inputs together and encodes them with shared (coupled) trainable parameters, is significantly more accurate with coupled multiphysics (thermo-electrical) analysis data than S-DeepONet MIONet with two branches, and this is particularly the case for electrical potential, where MIONet-based S-DeepONet has over 15% error. In contrast, the single-branch S-DeepONet has slightly over 1% error.

On the other hand, uncoupled data represents a significantly less challenging task for prediction, and both architectures are pretty accurate. Since each physics depends on its input only, the two-branch (MIONet-based) S-DeepONet model is slightly more accurate by reading and encoding each input separately and joining them via the Hadamard tensor product.

Table 1: Mean  $L_2$  relative errors for Temperature.

$L_2$ relative error [%]	Single-Branch	Two-Branch (MIONet)
Coupled Physics	<b>0.50</b>	6.61
Uncoupled Physics	0.13	<b>0.07</b>

Table 2: Mean  $L_2$  relative errors for Electrical Potential.

$L_2$ relative error [%]	Single-Branch	Two-Branch (MIONet)
Coupled Physics	<b>1.10</b>	15.5
Uncoupled Physics	0.10	<b>0.08</b>

### 3.3 Multiphysics: Thermo-Mechanical Model

Owing to the extensive range of prescribed thermal and displacement histories imposed as boundary conditions on the chilled edge, steel solidification in the continuous caster is periodically impeded, resulting in the domain predominantly remaining in the liquid and mushy zones, characterized by negligible strength and minimal, nearly constant stress magnitudes. These instances lack significance in stress-based casting failure forecasts and exemplify outlier targets that are difficult to forecast using machine learning methods. Consequently, the mean absolute error (MAE) measure in Equation 11, calculated between the finite element (target) and predicted solution values across all testing samples  $N$ , offers superior interpretability compared to relative errors, which involve division by small stress norm values in predominantly liquid and mushy zones. Furthermore, the findings are provided within the 85-90% test error range for both stress and temperature data to mitigate the impact of near-zero stress outliers.

$$MAE = \frac{1}{N} \sum_{i=1}^N |S_{FE,i} - S_{pred,i}| \quad (11)$$

Figure 11 compares predicted and target temperature values, and Figure 12 shows stress at the mold exit along the slice domain for coupled multiphysics data for single-branch and two-branch (MIONet) S-DeepONet models. Temperature distributions are inherently smoother and less challenging for both S-DeepONet implementations to predict than the stress distribution. The most unfavorable test case forecasted the complete temperature distribution with an absolute error of 0.65 °C, which is highly precise given that the steel temperatures in continuous casting molds range from 1000 °C to 1500 °C. Stress distributions are significantly affected by the three constitutive models (austenite, delta-ferrite, and mushy/liquid) determined by the prevailing phase fractions and temperature throughout the solidification process. Furthermore, stress is contingent upon temperature fluctuations due to thermal fluxes and the changing displacement history applied to the cooled surface. This results in a highly erratic stress distribution across the slice domain, complicating precise prediction. Despite the evident challenges, both S-DeepONet implementations relatively accurately predicted stress distribution, including stress reversals with tensile stress at the chilled surface, with test errors of 45% and 85% in samples. These are crucial for forecasting certain failure mechanisms, such as hot tearing. Between the two models, single-branch S-DeepONet was more accurate with stress MAE of 0.12 MPa vs. 0.23 MPa for two-branch S-DeepONet. This is particularly evident in the 85% test error, where the two-branch prediction deviated from the target, and the single-branch prediction remained consistent throughout the entire solid phase.

The histogram of test error distributions in Figure 13 further emphasizes the accuracy of single-branch implementation over two-branch implementation, particularly for stress, where two-branch stress predictions (blue columns) have a long tail into larger error areas.

Similarly to the thermo-electric model, the uncoupled data model with a single-temperature solution passed into the stress model represents a significantly less challenging case for predicting stress distribution, as stress in this case only depends on the displacement input. The corresponding histogram of test errors in Figure 14 reveals that the data from that uncoupled dual physics slightly favors the 2-branch (MIONet) model, which reads and encodes thermal and mechanical inputs separately.

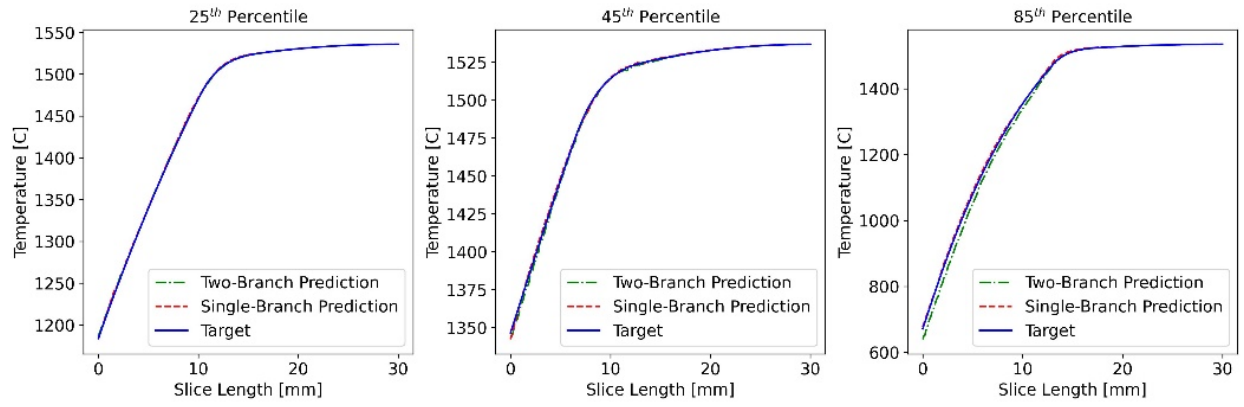


Figure 11: Temperature Comparison, Coupled Thermo-Mechanical Physics

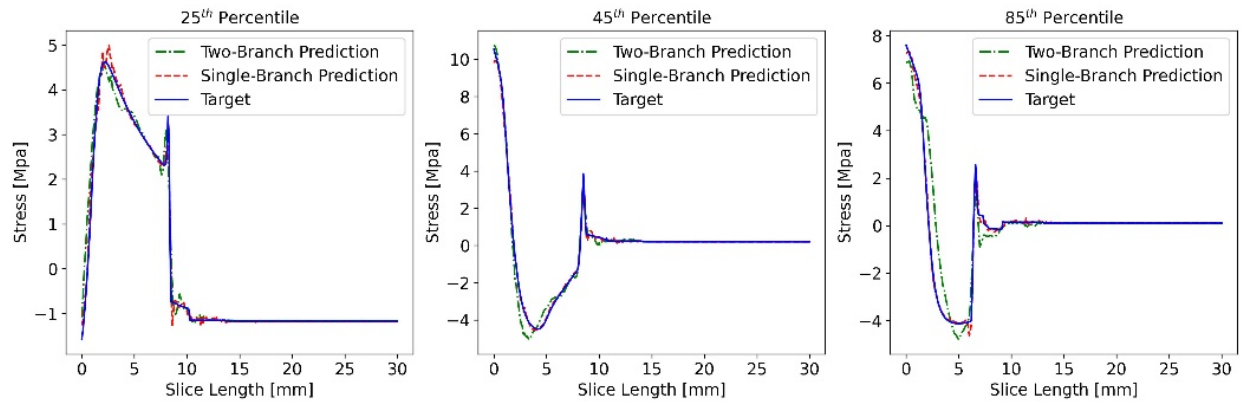


Figure 12: Stress Comparison, Coupled Thermo-Mechanical Physics

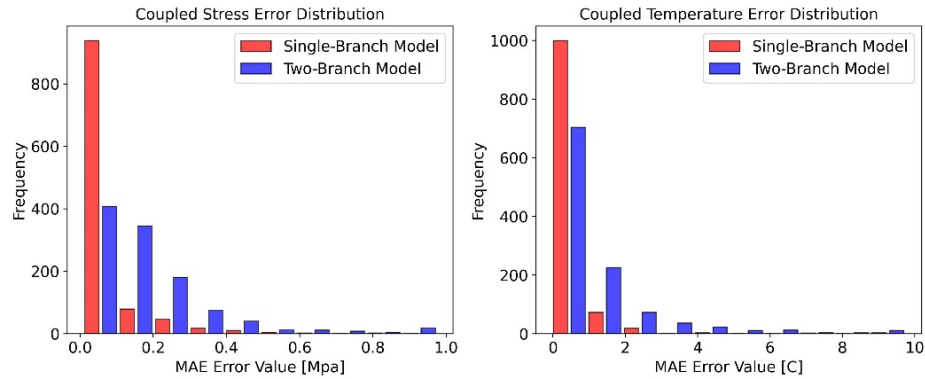


Figure 13: Histogram of Test Errors, Coupled Thermo-Mechanical Physics

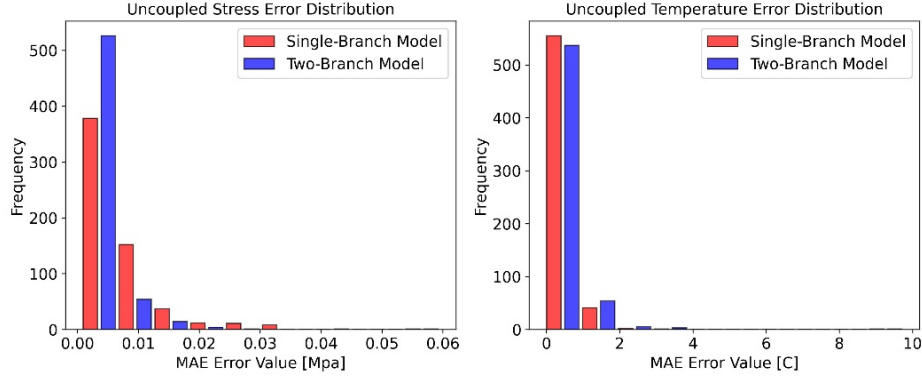


Figure 14: Histogram of Test Errors, Uncoupled Thermo-Mechanical Physics

Tables 3 and 4 summarize thermo-mechanical MAE error results. The single-branch S-DeepONet, which reads both inputs together and encodes them with shared (coupled) trainable parameters, is more accurate with coupled multiphysics (thermo-mechanical) analysis data. On the other hand, the two-branch (MIONet-based) S-DeepONet model, which reads and encodes each input separately and joins them via Hadamard tensor product, is slightly more accurate for uncoupled physics model data, where each physics depends on its input only.

Table 3: Stress MAE Errors.

Stress MAE [MPa]	Single-Branch	Two-Branch (MIONet)
Coupled Physics	<b>0.12</b>	0.23
Uncoupled Physics	0.09	<b>0.05</b>

Table 4: Temperature MAE Errors.

Stress MAE [MPa]	Single-Branch	Two-Branch (MIONet)
Coupled Physics	<b>0.91</b>	1.56
Uncoupled Physics	0.77	0.75

Some performance metrics observed during the training of the reaction-diffusion and thermo-mechanical models on an A100 Nvidia GPU with optimized hyperparameters are provided in Table 5.

The DeepONet architecture, which utilizes fully connected (FNN) networks, requires a relatively large number of trainable parameters to achieve the highest prediction accuracy for the reaction-diffusion case. And even though the multi-branch (MIONet) variant has almost twice the number of trainable parameters, due to highly optimized FNN kernels on the GPU, it did not result in larger training times.

As expected, for the thermo-mechanical solidification case, S-DeepONet performs recurrent neural network operations in the GRU-based branches and therefore requires a longer training time and a larger number of epochs to achieve high prediction accuracy. However, it was able to complete the entire training in 1.4 hours for a single-branch S-DeepONet and in 2.8 hours for a multi-branch (MIONet) DeepONet. This is particularly encouraging for the single-branch DeepONet, which not only provides more efficient training but also achieves higher accuracy for coupled multiphysics problems.

Finally, since DeepONets are typically trained only once and don't require additional training or transfer learning, it is even more important to evaluate the inference times, particularly in comparison with the cost of classical numerical analysis. The trained S-DeepONet thermo-mechanical models required 20. and 23. seconds to predict all stress and temperature fields for 1,099 test samples, resulting in prediction times of 0.0185 and 0.020 seconds per unseen sample for single-branch and two-branch models, respectively. The coupled finite element analysis (FEA) utilizing a highly optimized commercial FEA algorithm and a parallel solver on the latest high-performance computing (HPC) system required 333 seconds, as depicted in Figure 15. Thus, predicting the trained neural networks for prediction exhibits an extraordinary speed enhancement, almost 18,000 times faster!

Table 5: Training Performance.

Model (Architecture)	Single-Branch		Multiple-Branch (MIONet)	
	Trainable Params	Train Time (Epochs)	Trainable Params	Train Time (Epochs)
ReactDiff (DON)	1.25 M	600 sec (110,000)	2.5 M	658 sec (110,000)
Ther-Mech (S-DON)	0.8 M	5,172 sec (300,000)	1.5 M	9,931 sec (300,000)

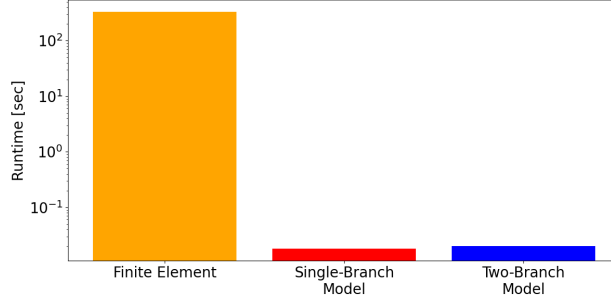


Figure 15: Runtime Comparison Between FEA and Trained S-DeepONet Models

## 4 Conclusions

This study presents the first systematic comparison of *single-branch* and *multi-branch* Deep Operator Networks—spanning both the classical and sequential (GRU-based S-DeepONet) formulations—across problems of increasing physical complexity, from single-physics to strongly coupled multiphysics regimes. The results yield three central insights:

1. **Architectural design must reflect physical coupling.** For strongly coupled systems, such as thermo-electrical and thermo-mechanical benchmarks, architectures that share parameters across all inputs (*single-branch*) consistently outperform factorized (*multi-branch*) (MIONet-style) designs. This advantage stems from their capacity to model nonlinear inter-field dependencies. In contrast, for weakly coupled or single-physics settings, *multi-branch* networks provide modest accuracy improvements due to their greater representational flexibility. This observation parallels classical distinctions between monolithic and partitioned solvers, now expressed through operator learning.
2. **Operator networks eliminate the runtime bottleneck.** Once trained offline, all evaluated models deliver full-field predictions in milliseconds, achieving up to four orders of magnitude speed-up compared to high-fidelity finite element solvers on modern high-performance computing infrastructure. This acceleration enables applications that were previously infeasible, including real-time digital twins, design-space exploration, and scalable uncertainty propagation.
3. **Guidelines for deployment.** The results provide actionable design principles: (i) shared-parameter branches should be the default for tightly coupled multiphysics problems, (ii) multi-branch encodings remain advantageous in decoupled or single-physics cases, and (iii) GPU-accelerated training makes operator models practical even for high-resolution, three-dimensional domains [65]. These guidelines form a foundation for the reliable deployment of operator surrogates in scientific workflows.

More broadly, this work demonstrates that neural operator architectures—when designed in alignment with the underlying physics—enable scalable, real-time surrogates for complex systems that have traditionally been beyond reach due to computational constraints. Extending these methods to irregular geometries, incorporating error bounds, and coupling them with optimization and control pipelines represent key directions for future research. Together, these advances position operator learning as a promising paradigm for efficient and interpretable modeling in multiphysics simulation and digital twin applications.



## Acknowledgments.

This research used the Delta advanced computing and data resource, which is supported by the National Science Foundation (award OAC 2005572) and the State of Illinois. Delta is a joint effort of the University of Illinois Urbana-Champaign and its National Center for Supercomputing Applications (NCSA). In addition, this work was supported in part by resources from the Illinois Computes project, a joint initiative of the University of Illinois Urbana-Champaign and the University of Illinois System. The authors would also like to thank NCSA at the University of Illinois, particularly its Research Consulting Directorate, and the Center for Artificial Intelligence Innovation (CAII) for their support.

## Disclosure of Interests.

The authors have no competing interests to declare that are relevant to the content of this article.

## Replication of Results.

The data and source code supporting this study will be available in the public GitHub repository <https://github.com/ncsa/MultiInputOperator> after the paper's acceptance.

## Declaration of AI-assisted technologies in the writing process

During the preparation of this work, the author(s) used ChatGPT for language editing and refinement. After using this tool/service, the author(s) reviewed and edited the content as needed and take full responsibility for the content of the publication.

## References

- [1] Kazuma Kobayashi et al. Ai-driven non-intrusive uncertainty quantification of advanced nuclear fuels for digital twin-enabling technology. *Progress in Nuclear Energy*, 172:105177, 2024.
- [2] Stefano Pagani and Andrea Manzoni. Enabling forward uncertainty quantification and sensitivity analysis in cardiac electrophysiology by reduced order modeling and machine learning. *International Journal for Numerical Methods in Biomedical Engineering*, 37(6):e3450, 2021.
- [3] Shantanu Shahane, Erman Guleryuz, Diab W Abueidda, Allen Lee, Joe Liu, Xin Yu, Raymond Chiu, Seid Koric, Narayana R Aluru, and Placid M Ferreira. Surrogate neural network model for sensitivity analysis and uncertainty quantification of the mechanical behavior in the optical lens-barrel assembly. *Computers & Structures*, 270:106843, 2022.
- [4] Qibang Liu, Diab Abueidda, Sagar Vyas, Yuan Gao, Seid Koric, and Philippe H Geubelle. Adaptive data-driven deep-learning surrogate model for frontal polymerization in dicyclopentadiene. *The Journal of Physical Chemistry B*, 128(5):1220–1230, 2024.
- [5] Shashank Kushwaha, Jaewan Park, Seid Koric, Junyan He, Iwona Jasiuk, and Diab Abueidda. Advanced deep operator networks to predict multiphysics solution fields in materials processing and additive manufacturing. *Additive Manufacturing*, 88:104266, 2024.
- [6] Elyas Goli, Sagar Vyas, Seid Koric, Nahil Sobh, and Philippe H Geubelle. Chemnet: A deep neural network for advanced composites manufacturing. *The Journal of Physical Chemistry B*, 124(42):9428–9437, 2020.
- [7] Hunter T Kollmann, Diab W Abueidda, Seid Koric, Erman Guleryuz, and Nahil A Sobh. Deep learning for topology optimization of 2d metamaterials. *Materials & Design*, 196:109098, 2020.
- [8] Jan-Hendrik Bastek and Dennis M Kochmann. Inverse design of nonlinear mechanical metamaterials via video denoising diffusion models. *Nature Machine Intelligence*, 5(12):1466–1475, 2023.
- [9] Maziar Raissi, Paris Perdikaris, and George E Karniadakis. Physics-informed neural networks: A deep learning framework for solving forward and inverse problems involving nonlinear partial differential equations. *Journal of Computational physics*, 378:686–707, 2019.
- [10] Luning Sun, Han Gao, Shaowu Pan, and Jian-Xun Wang. Surrogate modeling for fluid flows based on physics-constrained deep learning without simulation data. *Computer Methods in Applied Mechanics and Engineering*, 361:112732, 2020.



- [11] Junyan He, Diab Abueidda, Rashid Abu Al-Rub, Seid Koric, and Iwona Jasiuk. A deep learning energy-based method for classical elastoplasticity. *International Journal of Plasticity*, 162:103531, 2023.
- [12] Jan N Fuhg and Nikolaos Bouklas. The mixed deep energy method for resolving concentration features in finite strain hyperelasticity. *Journal of Computational Physics*, 451:110839, 2022.
- [13] Vien Minh Nguyen-Thanh, Xiaoying Zhuang, and Timon Rabczuk. A deep energy method for finite deformation hyperelasticity. *European Journal of Mechanics-A/Solids*, 80:103874, 2020.
- [14] Aditi Krishnapriyan, Amir Gholami, Shandian Zhe, Robert Kirby, and Michael W Mahoney. Characterizing possible failure modes in physics-informed neural networks. *Advances in neural information processing systems*, 34:26548–26560, 2021.
- [15] Sifan Wang, Xinling Yu, and Paris Perdikaris. When and why pinns fail to train: A neural tangent kernel perspective. *Journal of Computational Physics*, 449:110768, 2022.
- [16] Nikola Kovachki, Zongyi Li, Burigede Liu, Kamyar Azizzadenesheli, Kaushik Bhattacharya, Andrew Stuart, and Anima Anandkumar. Neural operator: Learning maps between function spaces with applications to pdes. *Journal of Machine Learning Research*, 24(89):1–97, 2023.
- [17] Tianping Chen and Hong Chen. Universal approximation to nonlinear operators by neural networks with arbitrary activation functions and its application to dynamical systems. *IEEE transactions on neural networks*, 6(4):911–917, 1995.
- [18] Kamyar Azizzadenesheli, Nikola Kovachki, Zongyi Li, Miguel Liu-Schiaffini, Jean Kossaifi, and Anima Anandkumar. Neural operators for accelerating scientific simulations and design. *Nature Reviews Physics*, 6(5):320–328, 2024.
- [19] Zhiwei Zhao, Changqing Liu, Yingguang Li, Zhibin Chen, and Xu Liu. Diffeomorphism neural operator for various domains and parameters of partial differential equations. *Communications Physics*, 8(1):15, 2025.
- [20] Zongyi Li, Hongkai Zheng, Nikola Kovachki, David Jin, Haoxuan Chen, Burigede Liu, Kamyar Azizzadenesheli, and Anima Anandkumar. Physics-informed neural operator for learning partial differential equations. *ACM/JMS Journal of Data Science*, 1(3):1–27, 2024.
- [21] Biao Yuan, He Wang, Yanjie Song, Ana Heitor, and Xiaohui Chen. High-fidelity multiphysics modelling for rapid predictions using physics-informed parallel neural operator. *arXiv preprint arXiv:2502.19543*, 2025.
- [22] Md Ashiqur Rahman, Robert Joseph George, Mogab Elleithy, Daniel Leibovici, Zongyi Li, Boris Bonev, Colin White, Julius Berner, Raymond A Yeh, Jean Kossaifi, et al. Pretraining codomain attention neural operators for solving multiphysics pdes. *Advances in Neural Information Processing Systems*, 37:104035–104064, 2024.
- [23] Zongyi Li, Nikola Kovachki, Kamyar Azizzadenesheli, Burigede Liu, Kaushik Bhattacharya, Andrew Stuart, and Anima Anandkumar. Fourier neural operator for parametric partial differential equations. *arXiv preprint arXiv:2010.08895*, 2020.
- [24] Chaoyu Liu, Davide Murari, Chris Budd, Lihao Liu, and Carola-Bibiane Schönlieb. Enhancing fourier neural operators with local spatial features. *arXiv preprint arXiv:2503.17797*, 2025.
- [25] Zipeng Xiao, Siqi Kou, Hao Zhongkai, Bokai Lin, and Zhijie Deng. Amortized fourier neural operators. *Advances in Neural Information Processing Systems*, 37:115001–115020, 2024.
- [26] Tapas Tripura and Souvik Chakraborty. Wavelet neural operator: a neural operator for parametric partial differential equations. *arXiv preprint arXiv:2205.02191*, 2022.
- [27] Xinliang Liu, Bo Xu, Shuhao Cao, and Lei Zhang. Mitigating spectral bias for the multiscale operator learning. *Journal of Computational Physics*, 506:112944, 2024.
- [28] Shaoxiang Qin, Fuyuan Lyu, Wenhui Peng, Dingyang Geng, Ju Wang, Naiping Gao, Xue Liu, and Liangzhu Leon Wang. Toward a better understanding of fourier neural operators: Analysis and improvement from a spectral perspective. *arXiv e-prints*, pages arXiv–2404, 2024.
- [29] Lu Lu, Pengzhan Jin, Guofei Pang, Zhongqiang Zhang, and George Em Karniadakis. Learning nonlinear operators via deepnet based on the universal approximation theorem of operators. *Nature machine intelligence*, 3(3):218–229, 2021.
- [30] Sifan Wang, Hanwen Wang, and Paris Perdikaris. Learning the solution operator of parametric partial differential equations with physics-informed deepnets. *Science advances*, 7(40):eabi8605, 2021.
- [31] Luis Mandl, Somdatta Goswami, Lena Lambers, and Tim Ricken. Separable physics-informed deepnet: Breaking the curse of dimensionality in physics-informed machine learning. *Computer Methods in Applied Mechanics and Engineering*, 434:117586, 2025.

- [32] Junyan He, Shashank Kushwaha, Jaewan Park, Seid Koric, Diab Abueidda, and Iwona Jasiuk. Sequential deep operator networks (s-deeponet) for predicting full-field solutions under time-dependent loads. *Engineering Applications of Artificial Intelligence*, 127:107258, 2024.
- [33] Seid Koric, Asha Viswantah, Diab W Abueidda, Nahil A Sobh, and Kamran Khan. Deep learning operator network for plastic deformation with variable loads and material properties. *Engineering with Computers*, 40(2):917–929, 2024.
- [34] Somdatta Goswami, Minglang Yin, Yue Yu, and George Em Karniadakis. A physics-informed variational deeponet for predicting crack path in quasi-brittle materials. *Computer Methods in Applied Mechanics and Engineering*, 391:114587, 2022.
- [35] Tun Zhao, Weiqi Qian, Jie Lin, Hai Chen, Houjun Ao, Gong Chen, and Lei He. Learning mappings from iced airfoils to aerodynamic coefficients using a deep operator network. *Journal of Aerospace Engineering*, 36(5):04023035, 2023.
- [36] Liang Xu, Haigang Zhang, and Minghui Zhang. Training a deep operator network as a surrogate solver for two-dimensional parabolic-equation models. *The Journal of the Acoustical Society of America*, 154(5):3276–3284, 2023.
- [37] Ehsan Haghighat, Umair bin Waheed, and George Karniadakis. En-deeponet: An enrichment approach for enhancing the expressivity of neural operators with applications to seismology. *Computer Methods in Applied Mechanics and Engineering*, 420:116681, 2024.
- [38] Kazuma Kobayashi, James Daniell, and Syed Bahaiddin Alam. Improved generalization with deep neural operators for engineering systems: Path towards digital twin. *Engineering Applications of Artificial Intelligence*, 131:107844, 2024.
- [39] Kazuma Kobayashi, Samrendra Roy, Seid Koric, Diab Abueidda, and Syed Bahaiddin Alam. From proxies to fields: Spatiotemporal reconstruction of global radiation from sparse sensor sequences. *arXiv preprint arXiv:2506.12045*, 2025.
- [40] Kazuma Kobayashi et al. Deep neural operator-driven real-time inference to enable digital twin solutions for nuclear energy systems. *Nature Scientific reports*, 14(1):2101, 2024.
- [41] Raisa Hossain, Farid Ahmed, Kazuma Kobayashi, Seid Koric, Diab Abueidda, and Syed Bahaiddin Alam. Virtual sensing-enabled digital twin framework for real-time monitoring of nuclear systems leveraging deep neural operators. *npj Materials Degradation*, 9(1):21, 2025.
- [42] Izzet Sahin, Christian Moya, Amirhossein Mollaali, Guang Lin, and Guillermo Paniagua. Deep operator learning-based surrogate models with uncertainty quantification for optimizing internal cooling channel rib profiles. *International Journal of Heat and Mass Transfer*, 219:124813, 2024.
- [43] Seid Koric and Diab W Abueidda. Data-driven and physics-informed deep learning operators for solution of heat conduction equation with parametric heat source. *International Journal of Heat and Mass Transfer*, 203:123809, 2023.
- [44] Sanghyun Lee and Yeonjong Shin. On the training and generalization of deep operator networks. *SIAM Journal on Scientific Computing*, 46(4):C273–C296, 2024.
- [45] Amanda A Howard, Mauro Perego, George Em Karniadakis, and Panos Stinis. Multifidelity deep operator networks for data-driven and physics-informed problems. *Journal of Computational Physics*, 493:112462, 2023.
- [46] Waleed Diab and Mohammed Al Kobaisi. U-deeponet: U-net enhanced deep operator network for geologic carbon sequestration. *Scientific Reports*, 14(1):21298, 2024.
- [47] Shengze Cai, Zhicheng Wang, Lu Lu, Tamer A Zaki, and George Em Karniadakis. Deepm&mnet: Inferring the electroconvection multiphysics fields based on operator approximation by neural networks. *Journal of Computational Physics*, 436:110296, 2021.
- [48] Zhiping Mao, Lu Lu, Olaf Marxen, Tamer A Zaki, and George Em Karniadakis. Deepm&mnet for hypersonics: Predicting the coupled flow and finite-rate chemistry behind a normal shock using neural-network approximation of operators. *Journal of computational physics*, 447:110698, 2021.
- [49] Zhongyi Jiang, Min Zhu, and Lu Lu. Fourier-mionet: Fourier-enhanced multiple-input neural operators for multiphase modeling of geological carbon sequestration. *Reliability Engineering & System Safety*, 251:110392, 2024.
- [50] Ning Liu, Xuxiao Li, Manoj R Rajanna, Edward W Reutzel, Brady Sawyer, Prahalada Rao, Jim Lua, Nam Phan, and Yue Yu. Deep neural operator enabled digital twin modeling for additive manufacturing. *arXiv preprint arXiv:2405.09572*, 2024.

- [51] Kazuma Kobayashi et al. Explainable, interpretable, and trustworthy AI for an intelligent digital twin: A case study on remaining useful life. *Engineering Applications of Artificial Intelligence*, 129:107620, 2024.
- [52] James Daniell et al. Digital twin-centered hybrid data-driven multi-stage deep learning framework for enhanced nuclear reactor power prediction. *Energy and AI*, 19:100450, 2025.
- [53] Kazuma Kobayashi and Syed Bahaiddin Alam. Deep neural operator driven real time inference for nuclear systems to enable digital twin solutions. *arXiv preprint arXiv:2308.07523*, 2023.
- [54] Changfan Yang, Lichen Bai, Yinpeng Wang, Shufei Zhang, and Zeke Xie. Multiphysics bench: Benchmarking and investigating scientific machine learning for multiphysics pdes. *arXiv preprint arXiv:2505.17575*, 2025.
- [55] Sebastian Müller, Lennart Schüller, Alraune Zech, and Falk Heße. Gstools v1. 3: a toolbox for geostatistical modelling in python. *Geoscientific Model Development*, 15(7):3161–3182, 2022.
- [56] Igor A Baratta, Joseph P Dean, Jørgen S Dokken, Michal Habera, Jack HALE, Chris N Richardson, Marie E Rognes, Matthew W Scroggs, Nathan Sime, and Garth N Wells. Dolfinx: the next generation fenics problem solving environment. *Preprint*, 2023.
- [57] Patrick F Kozlowski, Brian G Thomas, Jean A Azzi, and Hao Wang. Simple constitutive equations for steel at high temperature. *Metallurgical Transactions A*, 23:903–918, 1992.
- [58] Hong Zhu. Coupled thermo-mechanical finite-element model with application to initial solidification. *The University of Illinois at Urbana-Champaign*, 1996.
- [59] Seid Koric and Brian G Thomas. Efficient thermo-mechanical model for solidification processes. *International journal for numerical methods in engineering*, 66(12):1955–1989, 2006.
- [60] Dassault Systèmes. *Abaqus/Standard User’s Manual, Version 2022*. Dassault Systèmes Simulia Corp., Providence, RI, 2022. Accessed via licensed software documentation.
- [61] Matthew LS Zappulla, Seong-Mook Cho, Seid Koric, Hyoung-Jun Lee, Seon-Hyo Kim, and Brian G Thomas. Multiphysics modeling of continuous casting of stainless steel. *Journal of Materials Processing Technology*, 278:116469, 2020.
- [62] National Center for Supercomputing Applications (NCSA). Delta user documentation. <https://docs.ncsa.illinois.edu/systems/delta/en/latest/index.html>, 2025. Accessed: January 25, 2025.
- [63] Pengzhan Jin, Shuai Meng, and Lu Lu. Mionet: Learning multiple-input operators via tensor product. *SIAM Journal on Scientific Computing*, 44(6):A3490–A3514, 2022.
- [64] Lu Lu, Xuhui Meng, Zhiping Mao, and George Em Karniadakis. Deepxde: A deep learning library for solving differential equations. *SIAM review*, 63(1):208–228, 2021.
- [65] Junyan He, Seid Koric, Diab Abueidda, Ali Najafi, and Iwona Jasiuk. Geom-deeponet: A point-cloud-based deep operator network for field predictions on 3d parameterized geometries. *Computer Methods in Applied Mechanics and Engineering*, 429:117130, 2024.